Influence of initial slab dip, inter-plate coupling, and nonlinear rheology on dynamic weakening at the lithosphere-asthenosphere boundary

Vivek Bhavsar[1,2], Margarete Jadamec[1,2], and Matthew Knepley[1,3]

[1]Institute for Artificial Intelligence and Data Science, University at Buffalo, SUNY
[2]Geology Department, University at Buffalo, SUNY
[3]Department of Computer Science and Engineering, University at Buffalo, SUNY

Key Points:

- Decreasing inter-plate coupling leads to increased plate motion and dynamic LAB weakening, facilitating subduction and plate tectonics.
- Subducting plate velocity and thickness of weakened LAB zone are positively correlated due to nonlinear mantle viscosity.
- Plate velocity and thickness of dynamically weakened LAB peak over time for models with initial dip of 30° and weakest plate interface.

Corresponding author: Vivek Bhavsar, vbhavsar@buffalo.edu

Abstract

The slab dip and long-term coupling at the plate interface can vary both between and within subduction zones. How these variations affect the long-term subduction dynamics and mantle rheology is important for understanding plate tectonics and its evolution. This paper presents two-dimensional (2D) models that examine the surface plate velocity and dynamic weakening of the asthenosphere as a function of six values of plate interface coupling (3.1×10^{20}, 1×10^{21}, 3.1×10^{21}, 1×10^{22}, 3.1×10^{22}, 1.0×10^{23} $Pa{\cdot}s$) and three values of initial slab dip (30^o, 45^o, 60^o). The models use a composite viscosity in the upper mantle and were run for 2000 time-steps. The instantaneous results show subducting plate speed and dynamic weakening at the lithosphere-asthenosphere boundary (LAB) increase with decreasing inter-plate coupling, and peak for models with an initial dip of 45^o. For time-dependent models, subducting plate speed also increases with decreasing inter-plate coupling. However, models with an initial slab dip of 30^o produce the fastest subducting plate speeds over time. The thickness of the dynamically weakened LAB evolves over the course of subduction. The results indicate the subducting plate velocity is correlated not only with the imposed inter-plate coupling, but also with the dynamic weakening of the LAB region. The weaker the inter-plate coupling, the easier for the slab to descend into the mantle and dynamically weaken the asthenosphere due to the strain-rate dependent rheology. This reduced viscous resistance to slab sinking facilitates subducting plate and mantle flow over time, thus easing the subduction process of plate tectonics.

Plain Language Summary

At subduction zone plate boundaries, the down-going plate slides past the upper plate, with plate boundary coupling and the viscosity of the underlying mantle resisting the downward slab pull of the descending plate. However, how resistance at the plate interface affects the dynamic viscous resistance of the asthenosphere at the base of the tectonic plates (also referred to as the lithosphere-asthenosphere boundary (LAB)) is less understood. A suite of two-dimensional (2D) time-dependent models of subduction were run that varied the plate interface coupling and initial slab dip. The numerical models of subduction incorporate a laboratory-based strain-rate dependent viscosity for the mantle. High-performance computing is required, with each model run on 48 compute cores. The downgoing plate velocity and thickness of the dynamically weakened LAB increase with decreasing plate interface coupling. The results show that the surface plate velocity and dynamic weakening in LAB are positively correlated. The models indicate that dynamic weakening at the LAB can be affected by how coupled the downgoing and overriding plates are to each other and that the resulting LAB weakening is important for facilitating plate tectonics.

1 Introduction

The coupling between the downgoing and overriding plate along the subduction interface, as well as the coupling between a surface plate and underlying asthenosphere, are critical parameters controlling the instantaneous and time-dependent dynamics of plate tectonics on Earth (Forsyth & Uyeda, 1975; Lallemand et al., 2005; Billen, 2008; Gerya, 2011; Duarte et al., 2013). Resistance to subduction at the plate interface, as well as the viscous resistance of the asthenosphere to subduction, are key forces that counteract the driving force of the negative buoyancy of the slab (Forsyth & Uyeda, 1975; Lallemand et al., 2005; Billen, 2008; Duarte et al., 2015). However, the resisting forces are often conceptualized as independent parameters with respect to one another. Thus, how one resisting force may dynamically influence another resisting force is still not well understood (Andrews & Billen, 2009; Jadamec & Billen, 2010, 2012; Gao, 2018; Semple & Lenardic, 2021).

Similarly, the slab pull force is often conceptualized as a driving force subject to an independent resistance from a constant viscosity asthenosphere. However, numerical models using a non-linearly deforming mantle suggest dynamic feedback between variable asthenospheric viscosity and the slab (Tovish et al., 1978; Billen & Hirth, 2007). In addition, two-dimensional (2D) and three-dimensional (3D) time-dependent and instantaneous models using a composite viscosity suggest that the geometry of the slab may influence the extent and magnitude of lateral variability in asthenosphere's viscous support of the slab (Billen & Hirth, 2007; Jadamec & Billen, 2012; Jadamec, 2015, 2016b). Thus, the driving and resisting forces of subduction are likely dynamically connected, with the feedbacks playing a key role in the subduction process (Billen & Hirth, 2007; Stadler et al., 2010; Jadamec & Billen, 2012; Jadamec, 2015, 2016b; Yang & Gurnis, 2016; MacDougall et al., 2017; Gao, 2018; Semple & Lenardic, 2021). The purpose of this paper is to systematically examine the relative influence of and dynamic feedbacks between the initial slab dip, viscous coupling along the plate interface, and non-linear response of the mantle through a suite of instantaneous and time-dependent 2D subduction models using a non-linear rheology.

In nature, asymmetric down-welling is observed at subduction zones, wherein a down-going plate is preferentially subducted into the asthenosphere beneath an overriding plate (Uyeda & Kanamori, 1979; Bercovici, 2003; Gerya et al., 2008; Li et al., 2008; Hayes et al., 2018; Jadamec et al., 2018). Observations indicate the angle at which the slab subducts varies between subduction zones, as well as within a subduction zone (Jarrard, 1986; Lallemand et al., 2005; Syracuse & Abers, 2006; Hayes et al., 2018; Jadamec et al., 2018). For example, South America, Alaska and Mexico contain flat slab subduction segments while the Marianas subduction zone has a slab sinking at the angle greater than 70°(Gutscher et al., 2000; Lallemand et al., 2005; Hayes et al., 2018; Jadamec et al., 2018). These variations in dip can lead to differences in the spatial extent of inter-plate overlap, environment of stress, mantle deformation fabrics, and the magnitude of weakening of a non-linear asthenosphere (Wdowinski et al., 1989; Gutscher et al., 2000; Billen & Gurnis, 2001; Kneller & Van Keken, 2007; Wada & Wang, 2009; Capitanio & Faccenda, 2012; Jadamec, 2015; MacDougall et al., 2017).

At convergent plate boundaries undergoing subduction, the sinking of the down-going plate beneath the overriding plate is met with resistance by mechanical coupling between the plates along the plate interface (Shreve & Cloos, 1986; Huang et al., 1998; Tagawa et al., 2007; Capitanio, Stegman, et al., 2010; Agard et al., 2018). This requires that the composition, rock condition, or rheology of the lithosphere has to be such that the rigid plates become weak enough to locally allow the subducting plate to slide past the overriding plate, whilst maintaining the internal rigidity of the plate interior (Capitanio, Stegman, et al., 2010; Tagawa et al., 2007; Bercovici, 2003; Bercovici & Ricard, 2005; Lamb & Davis, 2003; Sharples et al., 2016). Different approaches have been implemented in numerical models to represent a plate interface that allows for the down-going plate to slide past the upper plate, including for example, a damage rheology, an interface with and without anisotropic frictional rheology, history dependent rheology with lubrication on top of the subducting plate, and imposed weak-zones (Bercovici & Ricard, 2005; Sobolev & Babeyko, 2005; Tagawa et al., 2007; Jadamec & Billen, 2012; Sharples et al., 2014; Jadamec, 2016b; Sharples et al., 2016). In a broad sense, the plate interface zone can be conceptualized as placing a throttle on the rate of subduction. However, how the resistance to subduction along the subduction interface may in turn influence the viscous resistance of the underlying asthenosphere is still an active area of research (Jadamec & Billen, 2012).

During subduction, the surface plates must descend through the lithosphere-asthenosphere boundary (LAB) before being fully immersed in the asthenosphere. Different methods such as surface wave tomography, body wave tomography, reverberation and converted phases, and a combination of them are commonly used to constrain the LAB depth and characteristics (Eaton et al., 2009; Rychert & Shearer, 2009; Romanowicz, 2009; Fischer

et al., 2010; Rychert et al., 2020; Richards et al., 2020; Hua et al., 2023). However, despite the fact that the LAB is expected to be ubiquitous around the Earth (because it separates the outer rheological layer of the Earth, the lithosphere, from the underlying asthenosphere), resolving the depth to the LAB, quantifying the thickness of the LAB zone, and determining exactly which parameters give the LAB its decoupling properties remain elusive (Eaton et al., 2009; Rychert & Shearer, 2009; Romanowicz, 2009; Fischer et al., 2010; Rychert et al., 2020; Richards et al., 2020).

The asthenosphere has relatively low viscosity with the respect to the lithosphere and, similar to the lithosphere, can exhibit seismic anisotropy related to deformation fabrics (Mitrovica & Forte, 2004; Long & Silver, 2008; Mao & Zhong, 2021; Adhikari et al., 2021). Numerical studies commonly use either a Newtonian, Non-Newtonian, or a composite viscosity for the rheology of the mantle. Comparison of models of corner flow dynamics show the inclusion of a non-Newtonian viscosity leads to thinning of the upper plate above the mantle wedge (van Keken et al., 2008). 2D composite viscosity models, which include the dynamic weakening effects of dislocation creep, also predict lateral variations in dynamic weakening of the asthenosphere (Billen & Hirth, 2007; Jadamec, 2016b) that can facilitate decoupled mantle flow velocity from that of the surface plates in subduction zones (Jadamec, 2016b; MacDougall et al., 2017; Billen & Arredondo, 2018). In addition, 3D modeling indicates that the toroidal flow around the slab edge can be enhanced in intensity when using a using a composite viscosity (Jadamec & Billen, 2010, 2012). Numerical models have also showed the trade-offs between the stress exponents in the non-Newtonian viscosity and the slab strength on global plate velocities (Stadler et al., 2010). Thus, numerical models suggest that the viscosity of the asthenosphere can have a first order impact on the subduction dynamics and that it can vary in space and time (Jadamec & Billen, 2012; Jadamec, 2015, 2016b; Yang & Gurnis, 2016; MacDougall et al., 2017; Gao, 2018; Semple & Lenardic, 2021).

2 Methods

Computational fluid dynamics (CFD) can be used to model the long-term solid-state creeping flow in the mantle (Moresi & Solomatov, 1995; Moresi et al., 1996; Zhong, 2006). On long-time scales, the Earth's mantle can be treated as a highly viscous fluid (McKenzie et al., 1974; Torrance & Turcotte, 1971). In this paper, we examine the plate interface coupling and initial slab dip to address the relative importance on the subduction plate velocity, dynamic asthenospheric weakening, and run-time for the non-Newtonian instantaneous and time-dependent models. Specifically, 18 time-dependent 2D models were run to test the relative effect of (a) three initial slab dip angles (30^o, 45^o, 60^o) and (b) six values of the upper bound on plate interface coupling (3.1×10^{20}, 1.0×10^{21}, 3.1×10^{21}, 1.0×10^{22}, 3.1×10^{22}, 1.0×10^{23} $Pa \cdot s$) on the surface plate motion and dynamic weakening in the asthenosphere (Table 1). The trade-off between the driving forces and the resisting forces, their evolution through time, and how nonlinear viscosity affects their independence is examined. The models were run with CitcomCU (Zhong, 2006), an open-source, parallel finite element program based on CITCOM (Moresi & Solomatov, 1995). The model mesh and the mapping of the initial thermal and weak zone structures onto the mesh were both generated with `TECT_Mod3D`, formerly SlabGenerator or SubductionGenerator (Jadamec & Billen, 2010, 2012; Jadamec, 2016b).

2.1 Viscous Flow Modeling and Governing Equations

The CFD model approximates the solution of the governing equations with the necessary boundary and/or initial conditions (Moresi & Solomatov, 1995; Zhong et al., 2015; May & Moresi, 2008). The open-source finite element code, CitcomCU, is used to solve the conservation of mass, momentum, and energy equations for thermo-mechanical con-

vection assuming incompressibility and the Boussinesq approximation:

$$\frac{\partial u_i}{\partial x_i} = 0 \tag{1}$$

$$-\frac{\partial \tau_{ij}}{\partial x_j} + \frac{\partial p}{\partial x_i} = \alpha \rho_0 g \lambda_i (T - T_0) \tag{2}$$

$$\frac{\partial T}{\partial t} + u_i \frac{\partial T}{\partial x_i} = \kappa \frac{\partial^2 T}{\partial x_j^2} \tag{3}$$

where x_i and t are the space coordinates and time, respectively, u_i is the velocity, and τ_{ij}, p, T, ρ, g, λ_i, and α are the stress tensor, pressure, temperature, density, gravitational acceleration, unit vector in the direction of gravity, and thermal expansion, respectively (Zhong, 2006; Moresi & Solomatov, 1995). κ is the coefficient of thermal diffusion, $\kappa = k/\rho c_p$, where k is the thermal conductivity, and c_p is the heat capacity at constant

Table 1: List of models run. α_i and η_{UB} are the initial slab dip and upper bound on viscosity at plate interface, respectively. V_{sp}, h_{d19}, $h_{d19.5}$, and D_{ST} are the average horizontal surface plate velocity of the downgoing plate, thickness of zone of dynamically weakened LAB viscosity below $1 \times 10^{19}\ Pa \cdot s$ at 13°, and thickness of zone of dynamically weakened LAB viscosity below $3.1 \times 10^{19}\ Pa \cdot s$ at 13°, and deepest depth of the slab tip, respectively. The subscript $_M$ indicates the maximum value achieved. T_p is the runtime per 2 compute nodes. Each compute node contains two processors with 12 cores per processor, making a total of 48 cores per job. The total hours per job is $T_p \times 48$.

Model Parameters Varied			*Instantaneous Results*			*Time-dependent Results*			
Model name	α_i°	η_{UB} $(Pa \cdot s)$	V_{sp} $(\frac{cm}{yr})$	h_{d19} (km)	$h_{d19.5}$ (km)	$(V_{sp})_M$ $(\frac{cm}{yr})$	$(h_{d19})_M$ (km)	$(D_{ST})_M$ (km)	T_p (hrs)
Slab30_fc25	30	1.0×10^{23}	0.12	0	0	0.27	0	280.00	38.40
Slab30_fc37	30	3.1×10^{22}	0.36	0	28	1.57	0	331.80	44.05
Slab30_fc50	30	1.0×10^{22}	0.71	0	58.80	9.57	86.80	531.79	62.83
Slab30_fc62	30	3.1×10^{21}	1.08	0	78.40	13.80	107.80	487.58	65.35
Slab30_fc75	30	1.0×10^{21}	1.51	0	93.80	21.10	128.80	584.71	72.06
Slab30_fc87	30	3.1×10^{20}	1.89	5.60	103.60	25.37	135.80	584.71	72.72
Slab45_fc25	45	1.0×10^{23}	0.92	8.40	92.40	1.14	15.40	331.80	44.18
Slab45_fc37	45	3.1×10^{22}	1.69	26.60	106.40	2.25	39.20	350.00	42.14
Slab45_fc50	45	1.0×10^{22}	2.43	39.20	116.20	3.41	54.60	366.01	45.83
Slab45_fc62	45	3.1×10^{21}	2.96	46.20	123.20	4.40	61.60	388.10	52.87
Slab45_fc75	45	1.0×10^{21}	3.44	50.40	126	6.44	67.20	457.18	59.31
Slab45_fc87	45	3.1×10^{20}	3.80	54.60	130.20	12.04	103.60	506.92	65.23
Slab60_fc25	60	1.0×10^{23}	0.44	0	82.60	0.64	4.20	337.40	38.10
Slab60_fc37	60	3.1×10^{22}	0.74	11.20	93.80	1.06	25.20	344.40	52.83
Slab60_fc50	60	1.0×10^{22}	1.07	25.20	106.40	1.46	36.40	351.40	47.72
Slab60_fc62	60	3.1×10^{21}	1.09	25.20	103.60	1.84	43.40	356.50	52.55
Slab60_fc75	60	1.0×10^{21}	1.77	40.60	120.40	2.23	49.00	360.80	45.04
Slab60_fc87	60	3.1×10^{20}	2.17	47.60	128.80	2.52	51.80	366.01	44.17

pressure (Zhong et al., 2015). CitcomCU uses the full multigrid (FMG) scheme to accelerate convergence (Zhong, 2006).

Table 2: Dimensionalization parameters

Parameter	Description	value
Ra	Rayleigh number	2.34×10^9
g	Gravitational Acceleration, m/s^2	9.8
T_0	Reference Temperature, K	1673
T_{surf}	Temperature on top surface, K	273
R	Earth radius, km	6371
η_{ref}	Reference viscosity, $Pa \cdot s$	10^{20}
ρ_0	Reference density, kg/m^3	3300
κ	Thermal diffusivity, m^2/s	10^{-6}
α	Thermal expansion coefficient, $1/K$	2×10^{-5}

The model uses a composite viscosity in the upper mantle and a Newtonian viscosity in the lower mantle. The viscosity is based on an experimentally derived flow law for olivine aggregates (Hirth & Kohlstedt, 2003)

$$\eta_{df,ds} = \left(\frac{d^p}{AC_{OH}^r} \right)^{\frac{1}{n}} \dot{\varepsilon}^{\frac{1-n}{n}} exp\left[\frac{E + P_l V}{n\widetilde{R}(T + T_{ad})} \right] \tag{4}$$

where η_{df} and η_{ds} are viscosity due to diffusion creep and dislocation creep respectively, $\widetilde{R}$ is the universal gas constant, T is a non-adiabatic temperature, T_{ad} is the adiabatic temperature, P_l is the lithostatic pressure, and the other parameters are as defined in Table 3.

For the diffusion creep of olivine, the strain-rate depends linearly on the stress but depends non-linearly on the grain size (Hirth & Kohlstedt, 2003). Whereas, for dislocation creep, the strain-rate depends non-linearly on the stress and does not depend on grain size (Hirth & Kohlstedt, 2003). Both dislocation creep and diffusion creep are sensitive to parameters including temperature, pressure, stain-rate, OH concentration, and grain size (Table 3, Eq. 4)(Hirth & Kohlstedt, 2003).

As diffusion and dislocation creep can occur simultaneously, and assuming the total strain rate is an additive contribution from each (Hall & Parmentier, 2003), the com-

Table 3: Creep parameters for wet olivine in the upper mantle used in the composite viscosity formulation (Hirth & Kohlstedt, 2003; Billen & Hirth, 2007).

Parameter	Description	Diffusion creep	Dislocation creep
A	Preexponential factor	1	9×10^{-20}
n	Stress exponent	1	3.5
d	Grain size, μm	10^4	-
p	Grain size exponent	3	-
C_{OH}	OH concentration, $H/10^6 Si$	1000	1000
r	C_{OH} exponent	1	1.2
E	Activation energy, KJ/mol	335	480
V	Activation volume, m^3/mol	4×10^{-6}	11×10^{-6}

posite viscosity, η_{comp}, (Hirth & Kohlstedt, 2004; Jadamec & Billen, 2010) can be defined by

$$\eta_{comp} = \frac{\eta_{df}\ \eta_{ds}}{\eta_{df} + \eta_{ds}}. \quad (5)$$

The models also use a depth-dependent yield stress, σ_y, that linearly increases with depth at a gradient of 15 MPa per km. Thus, the overall effective viscosity η_{eff} is equal to η_{comp} if $\sigma_{II} < \sigma_y$, and $\frac{\sigma_y}{\dot{\varepsilon}_{II}}$ if $\sigma_{II} > \sigma_y$ (Billen & Hirth, 2007; Jadamec & Billen, 2010).

2.2 Model Design and Constitutive Equations

The model setup, mesh, and initial thermal structure are constructed with `TECT_Mod3D` (formerly SlabGenerator or SubductionGenerator (Jadamec & Billen, 2010; Jadamec et al., 2012)). `TECT_Mod3D` uses either a plate cooling or half-space cooling model, combined with diffusion length scale adjustments, to define the initial thermal structure.

2.2.1 Model Setup

18 time-dependent models (Fig. 1(a), Table 1) were run that tested 3 initial subduction angles (Fig. 1(b-d)) and 6 values of plate interface coupling (Fig. 1(e-j)). The model domain, mesh, initial thermal structure, and slab geometry are from Jadamec (2016b). The model includes an overriding plate, subducting plate, and a mantle. The 2D model domain spans from 0°-45° in longitude and 2500 km in depth (Jadamec, 2016b)). The top boundary (surface) and the bottom boundary of the model are located at 6371.13 km and at 3871.13 km respectively, calculated from the center of the Earth (Fig. 1(a)), forming a model thickness of 2500 km. The model has 1248×480 elements in the longitude and radial direction respectively, with locally a refined mesh in the subduction zone region (Jadamec, 2016b). In the longitudinal direction, the element size is 0.016° ($\sim$ 1.7 km) at the trench and it coarsens outwards to 0.1525° ($\sim$ 16 km). In depth, the element size is 1.4 km for the upper 350 km and coarsens to 15 km in the lower mantle.

The dimensionalization parameters for the models in CitcomCU are defined in Table 2. Free slip conditions are applied to the model top, bottom, and sidewalls and the top and bottom of the model have a fixed temperature boundary condition. The maximum temperature allowed inside of the model domain and at the mantle-core boundary is 1400 ^oC (non-dimensionalised temperature = 1). Therefore, we applied a temperature restriction in the Petrov-Galerkin time stepping function in the CitcomCU to cap the maximum temperature at 1.

The initial condition is required for temperature as the first-order time derivative is presented in the energy equation, Eq. 3. The initial thermal structure shown in Fig. 1(b-d) is proportional to the age of the overriding and subducting plates. The half-space cooling model is used in SlabGenerator (Jadamec & Billen, 2012) to determine the initial thermal field. This study uses three initial slab dips (30°, 45° and 60°) following Jadamec (2016b). Models with an initial slab dip of 30° have shallower slab depth at the start of subduction. At the start of the subduction, models with an initial slab dip of 45° have an intermediate slab depth while models with an initial slab dip of 60° have deeper slab depth (Jadamec, 2016b).

2.2.2 Plate Interface Shear Zone

The plate interface and the trailing edge of the subducting plate have an imposed weak-zone, η_{wk}, following the implementation in Jadamec et al. (2012); Jadamec (2009). The viscosity implemented at the interface is defined as

$$\eta_{wk} = \eta_{ref} 10^{[(log_{10}(\eta_{eff}/\eta_{ref}))(1-A_{wk})]} \quad (6)$$

where η_{wk} is a upper bound on the imposed weak-zone, η_{ref} is the reference viscosity, and A_{wk} is a scalar weak-zone field. $A_{wk} = 0$ means there is no imposed weak plate interface, whereas $A_{wk} = 1$ represents a fully imposed weak plate interface.

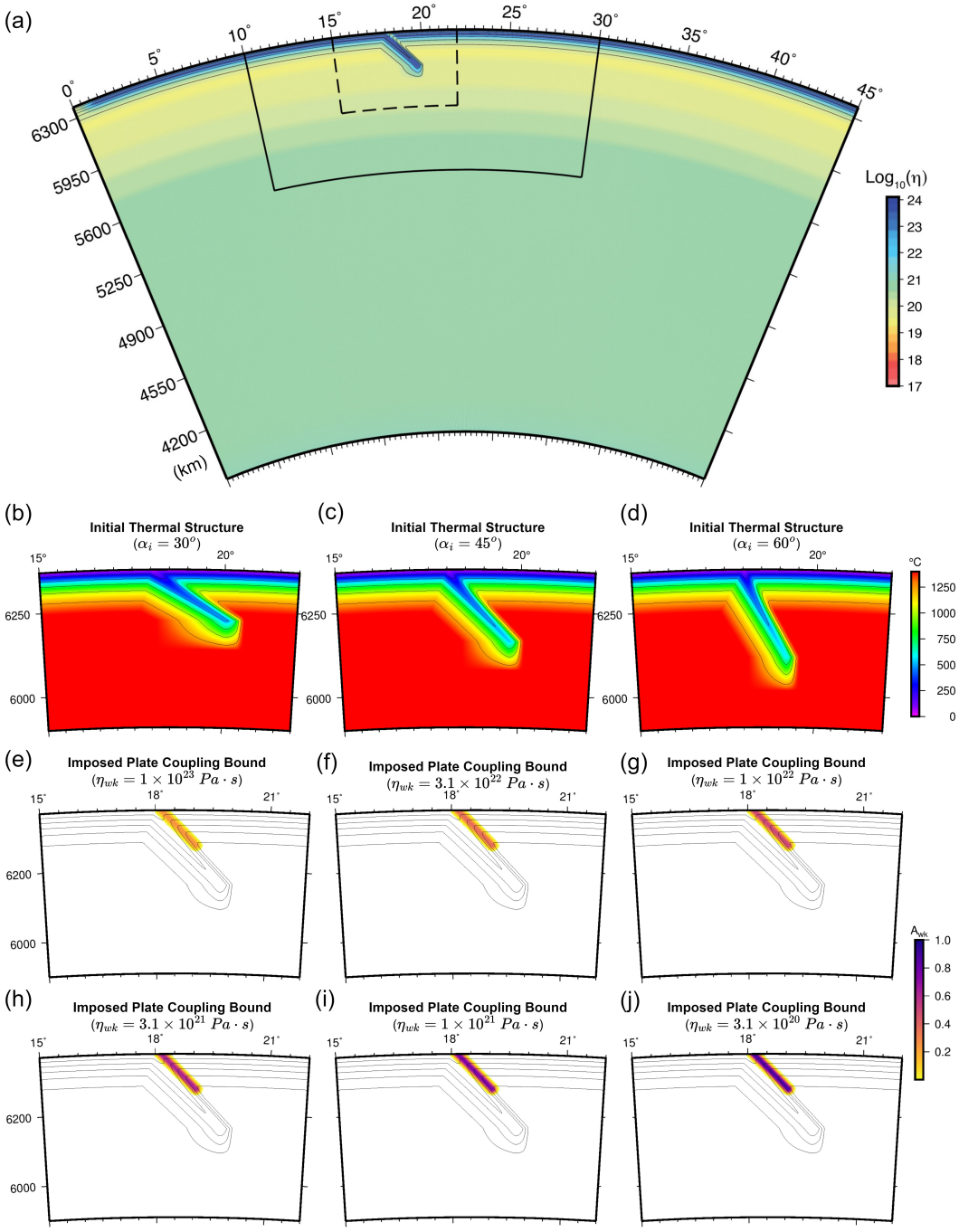

Figure 1: Model set-up. (a) Model domain, shown with Newtonian viscosity in color. Solid-line outlines zoomed-in region shown in results section. Dashed-line outlines zoomed-in region shown in model set-up (b-j). (b,c,d) Initial temperature from TECT_Mod3D input to CitcomCU for the three initial slab dips used, shown for subset of model domain. (e-j) Plate interface weak field from TECT_Mod3D input to CitcomCU plate for six plate coupling bounds used, shown for subset of model domain.

The weak-zone field, A_{wk}, is mapped on the mesh nodes a priori using a sigma function (Jadamec et al., 2012) (Fig. 1(e-j)). The 2D models presented here examined six different weak-zone fields along the plate interface. This parameter sweep is listed in Table 1, where column 2 represents the initial slab dip and column 3 represents the plate coupling bound in CitcomCU.

3 Results

The results of the instantaneous models and time dependent models are presented in Sections 3.1 and 3.2, respectively. The predicted flow velocity in the mantle, surface plate velocity, and thickness of the dynamically weakened asthenosphere are analyzed as functions of the initial slab dip and variable plate coupling.

3.1 Instantaneous Subduction Modeling Results

3.1.1 Newtonian Versus Composite Viscosity

Figure 2 shows a comparison of the flow velocity, strain rate, and viscosity for models using a Newtonian upper mantle versus a composite viscosity upper mantle. The viscosity for the models with the Newtonian viscosity formulation varies only with depth and does not dynamically weaken below 10^{19} $Pa{\cdot}s$ (Fig. 2(a), right). Models with the Newtonian viscosity formulation have smaller velocity gradients around the slab. Additionally, these models show lower magnitudes of velocity, as illustrated in Fig. 2(a). The strain-rate for this model is also smaller (Fig. 2(b)). In contrast, models using the composite viscosity formulation show faster velocity magnitudes, higher strain-rate, and a dynamically weakened viscosity, similar to previous results (Jadamec & Billen, 2010; Jadamec, 2016b) as shown in Figure 2(d-f). The mantle velocity magnitude is highest for composite viscosity models with an initial slab dip of 45°. In both Newtonian and composite viscosity models, large flow velocity gradients emerge in the asthenosphere around the slab and beneath the surface part of the down-doing plate in the lithosphere-asthenosphere boundary (LAB) region.

As many previous studies have already explored models using a Newtonian viscosity, all results hereafter are for the models using the composite viscosity upper mantle. We refer the reader to previous studies that examined comparisons with a Newtonian upper mantle rheology (Jadamec & Billen, 2010; Jadamec, 2016b), as this is beyond the scope of this paper.

3.1.2 Effect of Initial Slab Dip and Subduction Interface Coupling on Surface Plate velocity

The horizontal surface plate velocity is plotted as a function of imposed plate coupling bound for three initial slab dips in Fig. 3(a). The horizontal velocity on the surface grid nodes of the subducting plate is averaged to determine the average surface plate velocity. The surface plate velocity increases as the plate interface coupling decreases. Models with a plate interface bound of 1×10^{23} $Pa{\cdot}s$ have the slowest horizontal surface plate velocity ($0.1-0.9$ cm/yr) (Figures 3(a), 4(d-f)). Models with a plate interface bound of 3.1×10^{20} $Pa{\cdot}s$ have the fastest ($1.8-3.8$ cm/yr) surface plate velocity (Figures 3(a), 4(j-l)).

The results show that surface plate velocity is also sensitive to the initial slab dip (Figures 3(a) and 4). The surface plate velocity is slowest for models with an initial slab dip of 30°and is fastest for models with an initial slab dip of 45°. The difference in the speed for models with a slab dip of 45° is greater than for models with an initial slab dip of 30°. For models with an initial slab dip of 30°, the difference in surface plate velocity between the models with the strongest and weakest plate coupling is 1.76 cm/yr

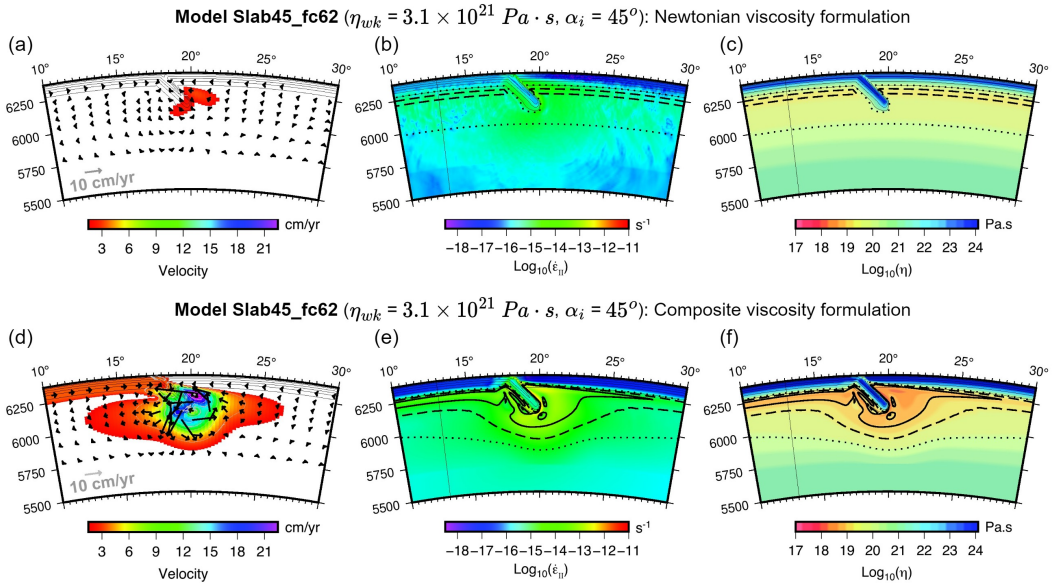

Figure 2: Instantaneous flow velocity magnitude, second invariant of strain-rate, and viscosity for model Slab45_fc62 with (a,b,c) Newtonian and (d,e,f) composite viscosity formulation for the upper mantle.

(93.7%). For models with an initial slab dip of 45°, the difference in surface plate velocity between the models with the strongest and weakest plate coupling reduces to 2.88 cm/yr (75.7%). For models with an initial slab dip of 60°, the difference in velocity between the models with the strongest and weakest plate coupling is 1.72 cm/yr (79.6%).

3.1.3 Effect of Initial Slab Dip and Plate Interface Coupling on Asthenospheric Viscosity

The mantle viscosity is dynamically reduced in the regions of high strain-rate around the slab and in the LAB region due to the effects of the composite viscosity formulation. Both the initial slab dip and plate interface coupling have an impact on the dimension and intensity of the zones of dynamic weakening. Overall, models with an initial slab dip of 45° achieved the highest amount of dynamic weakening (Fig. 4(h)). In addition, the zone of weakening around the slab and at the LAB is wider and thicker overall for models with the lowest plate interface bound (3.1×10^{20} $Pa{\cdot}s$) (Fig. 4(g-i)) and smaller for models with the highest plate interface bound (1 × 10^{23} $Pa \cdot s$) (Fig. 4(a-c)).

When the weakened asthenosphere in the sub-slab corner, below the slab tip, and in the mantle wedge is fully connected, a coherent envelope of low viscosity forms around the slab. We outline the coherence of the dynamic weakening in the asthenosphere with the 10^{19} $Pa \cdot s$ and 3.1 × 10^{19} $Pa \cdot s$ contours (Fig. 4). Table 4 shows the induced dynamic weakening ($\leq 10^{19}$ $Pa{\cdot}s$) in the sub-slab corner, mantle wedge, and beneath the slab tip for the instantaneous composite viscosity models. The rightmost column in Table 4 indicates whether there is weakening at the LAB region of the down-going plate. For models with a plate interface bound of 1×10^{23} $Pa{\cdot}s$, the zone of weakening is more coherent for the models with an initial slab dip of 45°and less coherent for models with an initial slab dip of 30° and 60°(Fig. 4(a-c)). For models with a plate interface bound of 3.1 × 10^{20} $Pa \cdot s$, models with an initial slab dip of 30° and 45° have the coherent zone of weakening (Fig. 4(g,h)). Models with an initial slab dip of 60° do not have weakening beneath the slab tip, regardless of plate coupling bound (Fig. 4(c,i)).

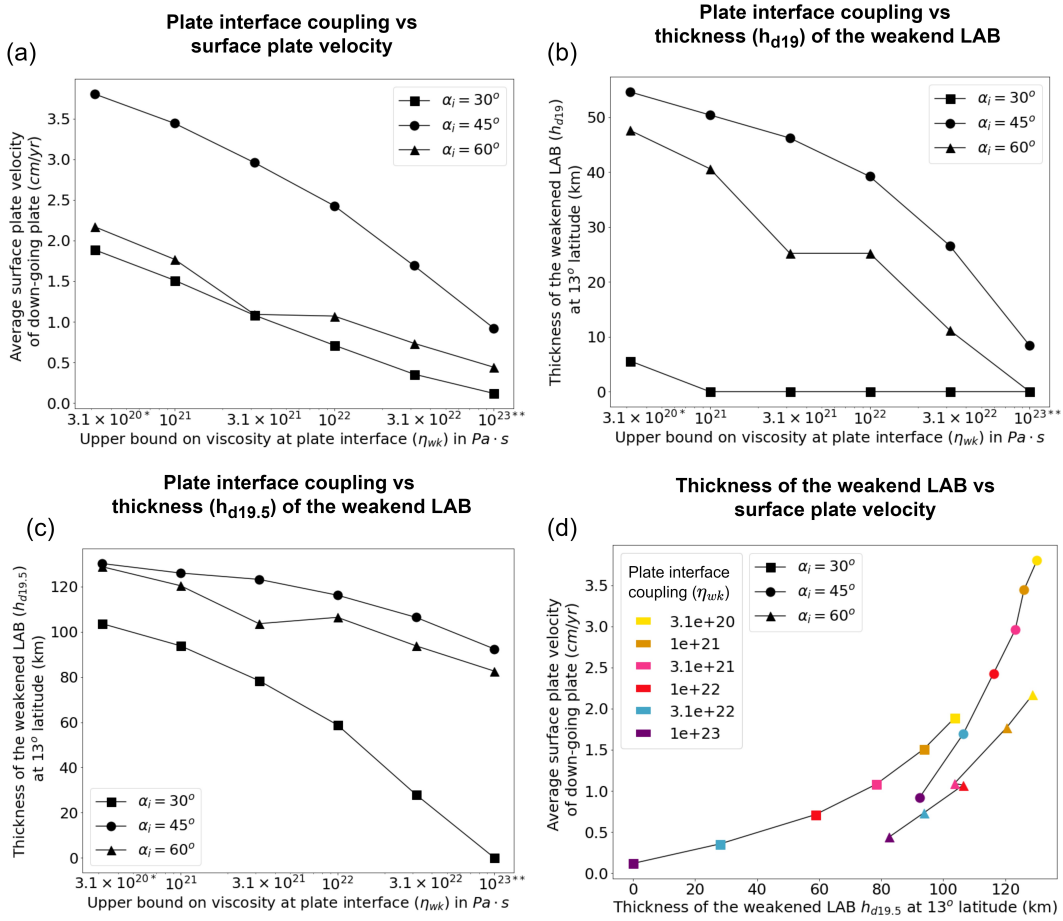

Figure 3: Predicted (a) surface plate velocity and (b, c) thickness of weakened asthenosphere to (h_{d19}) and ($h_{d19.5}$), respectfully, plotted as a function of imposed plate coupling bound for instantaneous models. (d) Predicted surface plate velocity plotted as a function of resulting $h_{d19.5}$ for instantaneous models. (**) case shown in Fig. 4(a-f) and (*) case shown in Fig. 4(g-l).

To examine the dynamic reduction in viscosity at the LAB beneath the down-going plate outboard of the trench, viscosity profiles at 13° latitude are extracted for all models (Figure 5). The profiles show the viscosity in the LAB is dynamically weakened below $3.1{\times}10^{19}$ $Pa{\cdot}s$ for all of the models with an initial slab dip of 45° and 60°(Figure 5). Models with an initial slab dip of 30° have a minimum viscosity less than $3.1{\times}10^{19}$ $Pa{\cdot}s$ for all of the models, except for the model with the strongest plate coupling. However, for models with an initial slab dip of 30°, the minimum viscosity is not below $1{\times}10^{19}$ $Pa{\cdot}s$ for all the models except for the model with the weakest plate coupling.

To further quantify the dynamically emergent weakening in the LAB region under the down-going plate, the thickness (h_{d19}) of the viscosity weakened below $1{\times}10^{19}$ $Pa{\cdot}s$ and 3.1×10^{19} $Pa \cdot s$ at 13° longitude is measured. The quantification of the thickness of the dynamically weakened region beneath the down-going plate at the LAB and surface plate velocity is as depicted in Figure 5(a). The thickness is plotted as a function of plate coupling in Fig. 3(b,c) for the three initial slab dips. The thickness of the weakened LAB area (h_{d19}) increases with decreasing plate coupling (8.3 km to 54.6 km for models with an initial slab dip of 45°) (Fig. 3(b)). Similarly, the thickness of the weak-

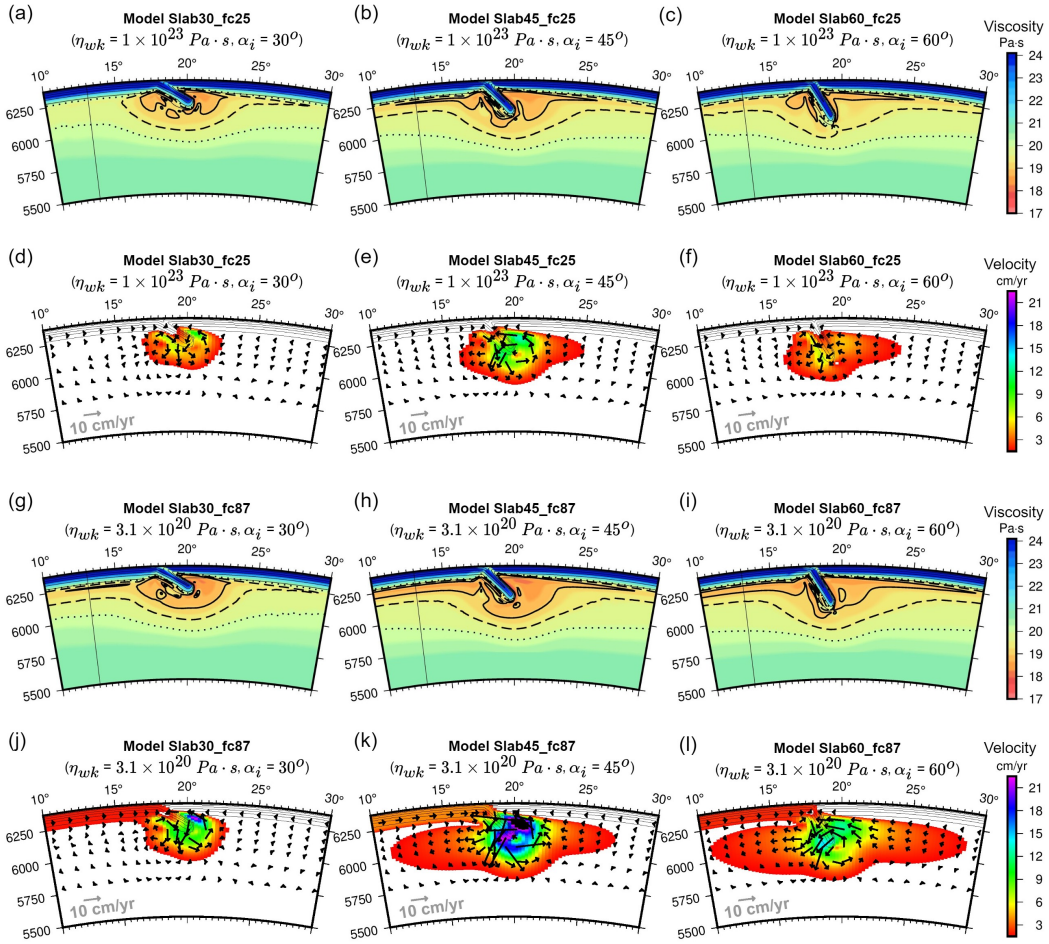

Figure 4: Viscosity (a,b,c) and velocity (d,e,f) results for instantaneous models with the strongest plate coupling and viscosity (g,h,i) and velocity (j,k,l) results for instantaneous models with the weakest plate coupling. Temperature contours (thin black lines), 1×10^{19} $Pa \cdot s$ viscosity contour (thick black line), 3.1×10^{19} $Pa \cdot s$ viscosity contour (thick dashed black line), 1×10^{20} $Pa \cdot s$ viscosity contour (dotted black line), and velocity vectors (black arrows) are shown.

ened LAB area ($h_{d19.5}$) considering the viscosity below 3.1×10^{19} $Pa \cdot s$ increases with decreasing plate coupling (Fig. 3(c)). However, the $h_{d19.5}$ is up to an order of magnitude thicker than the h_{d19}. For models with an imposed plate interface bound of 3.1×10^{20} $Pa \cdot s$, models with an initial slab dip of 45° have the thickest LAB area ($h_{d19} = 54.6$ km), and models with an initial slab dip of 30° have the thinnest thickness of weakened LAB area ($h_{d19} = 5.6$ km). The difference in the thickness of the weakened as-

Table 4: Regions of dynamically induced weakening below 10^{19} $Pa \cdot s$ in the instantaneous models using the composite viscosity.

Models	Weakening in sub-slab corner	Weakening in mantle wedge	Weakening beneath the slab tip	Coherent envelope	Weakening at the LAB region of the down-going plate
Slab30_fc25	Yes	Yes	Yes	No	No
Slab30_fc37	Yes	Yes	Yes	No	No
Slab30_fc50	Yes	Yes	Yes	No	No
Slab30_fc62	Yes	Yes	Yes	No	No
Slab30_fc75	Yes	Yes	Yes	Yes	No
Slab30_fc87	Yes	Yes	Yes	Yes	Yes
Slab45_fc25	Yes	Yes	Yes	Yes	Yes
Slab45_fc37	Yes	Yes	Yes	Yes	Yes
Slab45_fc50	Yes	Yes	Yes	Yes	Yes
Slab45_fc62	Yes	Yes	Yes	Yes	Yes
Slab45_fc75	Yes	Yes	Yes	Yes	Yes
Slab45_fc87	Yes	Yes	Yes	Yes	Yes
Slab60_fc25	Yes	Yes	No	No	No
Slab60_fc37	Yes	Yes	No	No	Yes
Slab60_fc50	Yes	Yes	No	No	Yes
Slab60_fc62	Yes	Yes	No	No	Yes
Slab60_fc75	Yes	Yes	No	No	Yes
Slab60_fc87	Yes	Yes	No	No	Yes

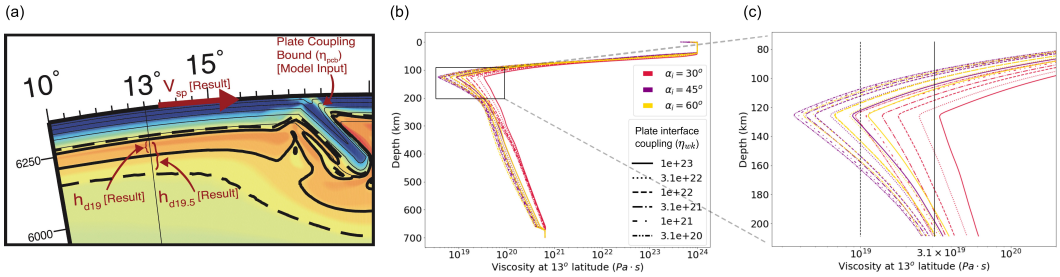

Figure 5: (a) Diagram illustrating input plate coupling bound and output quantities measured. Viscosity envelope (thick solid and dashed lines) shown in Figs. 2, 4, and 6. Viscosity profiles through all the models at 13° latitude to 700 km depth (b) show dynamic weakening in the LAB beneath the subducting plate with (c) zoomed-in plot of LAB region. Vertical solid and dashed black lines in (c) mark viscosity of 3.1×10^{19} and 1×10^{19} $Pa \cdot s$, respectively.

thenosphere (h_{d19}) between the models with the weakest and strongest plate coupling is larger for models with an initial slab dip of 45° and 60° than for models with an initial slab dip of 30°. For models using an initial slab dip of 30°, only the model with the weakest plate coupling ($3.1{\times}10^{20}$ $Pa{\cdot}s$) was able to achieve the viscosity below 10^{19} $Pa{\cdot}s$ and achieved only a 5.6 km thickness (h_{d19}). In addition, models with an initial slab dip of 30°, except for the model with the weakest interface coupling (3.1×10^{20} $Pa \cdot s$), failed to get weakened below 1×10^{19} $Pa \cdot s$.

3.2 Time-dependent Subduction Modeling Results

The time-dependent results show that asthenospheric flow velocity, the surface plate velocity, and the thickness of the dynamically weakened LAB area vary in time. For models with a plate interface coupling of 1×10^{23} $Pa \cdot s$, the mantle velocity speeds up for models with an initial slab dip of 30° and 60° through time (Movie S1 (b)). For models with a plate interface coupling of 1×10^{23} $Pa \cdot s$ and an initial slab dip of 45°, the mantle velocity is faster initially, however, the mantle velocity gets slower through time (Movie S1 (b)). In addition, the coherence of dynamic weakening around the slab varies in lateral extent through time (Supp. Info, Movie S1; Fig. 6). The effects of an initial slab dip and plate interface coupling on the surface plate velocity (Section 3.2.1), coherent zone of weakening (Section 3.2.2), and dynamic weakening at LAB area (Section 3.2.3) are described in the following subsections.

3.2.1 Effect of Initial Slab Dip and Subduction Interface Coupling on Surface Plate Velocity over Time

The surface plate velocity for all models with an initial slab dip of 30° increases through time except for the models with strongest imposed plate coupling bounds ($1{\times}$ 10^{23} $Pa \cdot s$) (Fig. 7(a)). The surface plate velocity for models with an initial slab dip of 30° increases more rapidly for models with weaker plate coupling bounds. The model with an initial dip of 30° and a weakest plate coupling achieved more than 20 cm/yr surface plate speed. Unlike in the instantaneous results, the surface plate velocity is fastest over time for models with an initial slab dip of 30°(Fig. 7(a)). The surface plate velocity for models with an initial slab dip of 45° increases with time for the models with the three weakest interface coupling bounds; whereas, the surface plate velocity decreases through time for the models with the three strongest plate coupling bounds (Fig. 7(c)). The surface plate velocity for all models with an initial slab dip of 60° decreases through time (Fig. 7(e)). Models with an initial slab dip of 60° have the lowest speed compared to models with an initial slab dip of 30° and 45°.

3.2.2 Effect of Initial Slab Dip and Plate Interface Coupling on Asthenospheric Viscosity over Time

The amount of weakening at the LAB increases over time for models with the weakest plate coupling and an initial slab dip of 30° and 45°(Movie S1 (c)). For models with the weakest plate coupling and an initial slab dip of 30° and 45°, the dynamic weakening in the sub-slab corner and in the mantle wedge increases and then decreases over time. The coherent envelope of low viscosity becomes incoherent over time for models with the weakest plate coupling and an initial slab dip of 30° and 45°. For model with the weakest plate coupling model and an initial slab dip of 60°, the dynamic weakening at the LAB, in the sub-slab corner, and in the mantle wedge decreases over time (Movie S1 (c)). Model with the weakest plate coupling model and an initial slab dip of 60°do not have dynamic weakening beneath the slab tip. The envelope of low viscosity stays incoherent throughout the process of subduction. For models with the strongest plate coupling, the dynamic weakening in the sub-slab corner and in the mantle wedge decreases over time (Movie S1 (a)). Models with the strongest plate coupling and an initial slab dip of

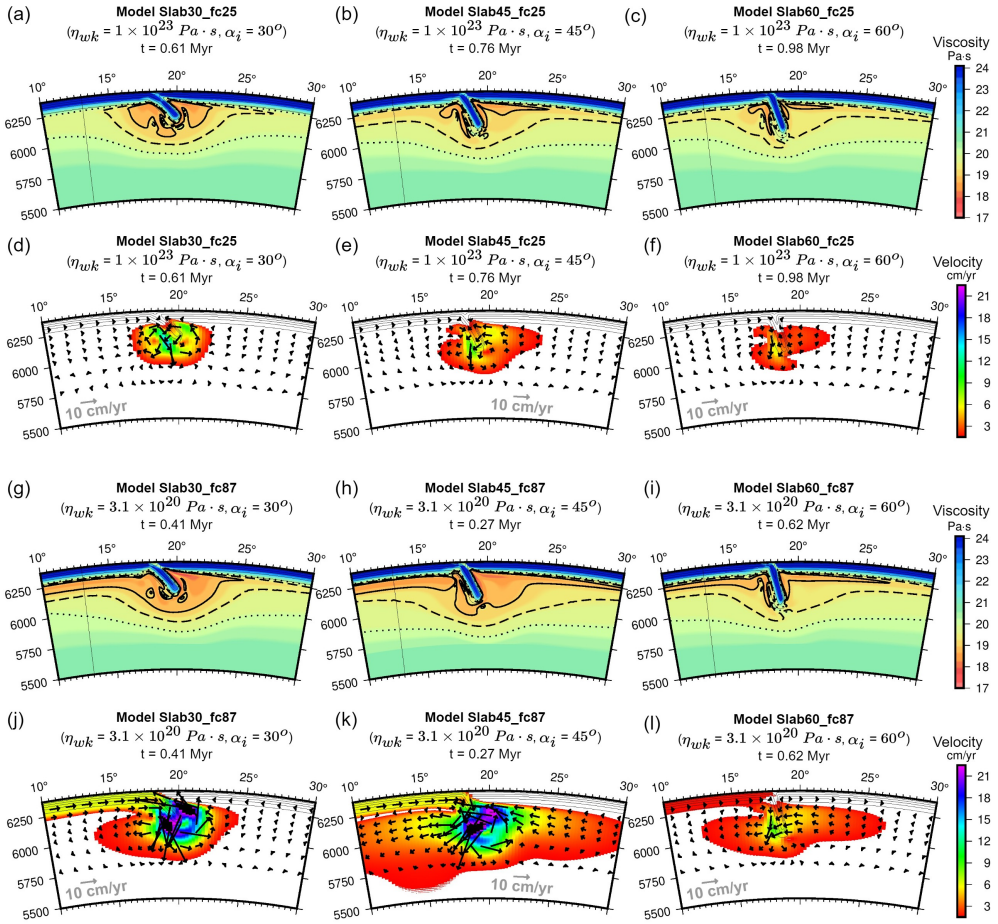

Figure 6: Viscosity (a,b,c) and velocity (d,e,f) for models with the strongest plate interface coupling and viscosity (g,h,i) and velocity (j,k,l) for models with the weakest plate interface coupling results for subset of models at time-step = 200. Temperature contours (thin black lines), 1×10^{19} $Pa \cdot s$ viscosity contour (thick black line), 3.1×10^{19} $Pa \cdot s$ viscosity contour (thick dashed black line), 1×10^{20} $Pa \cdot s$ viscosity contour (dotted black line), and velocity vectors (black arrows) are shown .

30° and 60°do not have dynamic weakening at the LAB below 10^{19} $Pa{\cdot}s$ through time. For model with the strongest plate coupling and an initial slab dip of 45°, the dynamic weakening at the LAB decreases over time. The envelope of low viscosity remains incoherent over time for models with the strongest plate coupling.

3.2.3 Effect of Initial Slab Dip and Subduction Interface Coupling on Weakening in LAB over Time

Models with an initial slab dip of 30° have the thickest weakened LAB region through time (Fig. 7(a); Movie S1), with the model using the weakest plate coupling bound having the greatest thickness through time. In the models with an initial slab dip of 45°, the models with the 4 largest plate coupling bound eventually have the thickness of the weakened LAB reduced to zero. However, the thickness of the LAB region for the models with the two weakest plate coupling bounds becomes thicker through time (Fig. 7(c)). For models with an initial dip of 60°, the thickness of the weakened LAB area decreases

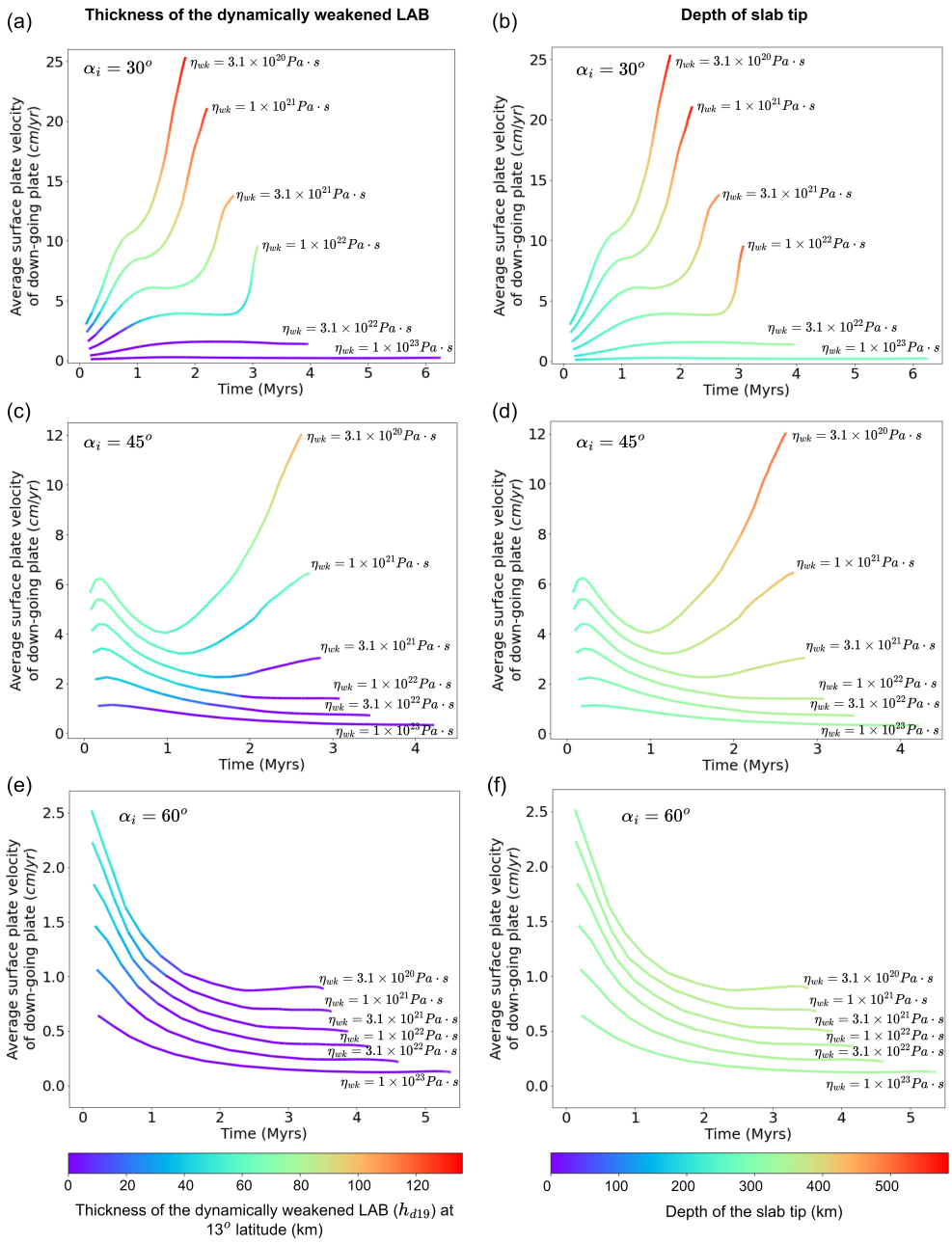

Figure 7: Surface plate velocity through time colored by the thickness of weakened LAB (a,c,e) and depth of the slab tip (b,d,f) for models with an initial slab dip of $\alpha_i = 30^o$, $\alpha_i = 45^o$, $\alpha_i = 60^o$, respectively, for all plate interface coupling values (3.1×10^{20}, 1.0×10^{21}, 3.1×10^{21}, 1.0×10^{22}, 3.1×10^{22}, 1.0×10^{23} $Pa \cdot s$).

through time and eventually goes to zero, regardless of plate coupling bound (Fig. 7(e); Movie S1). Regardless of the initial slab dip, the models with the strongest plate coupling do not weaken below 10^{19} $Pa \cdot s$ in the LAB region.

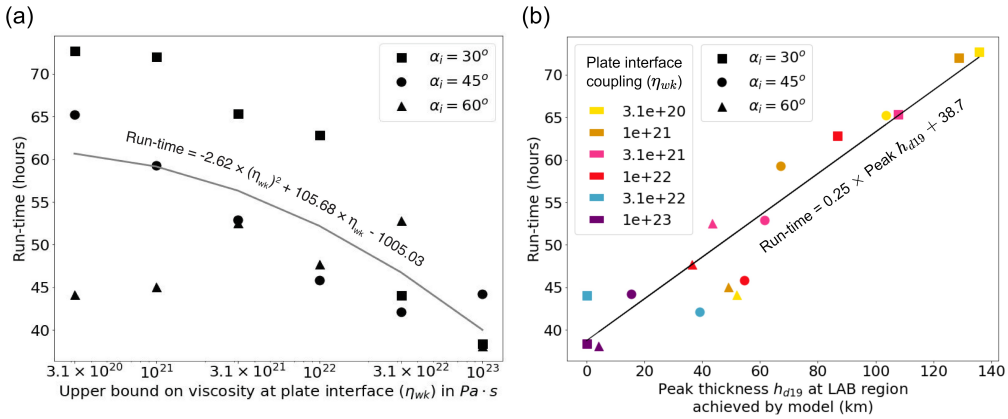

Figure 8: (a) Run-time per 2 compute nodes as a function of plate interface coupling values for time-dependent models. (b) Peak thickness h_{d19} achieved by each model plotted against run-time per 2 compute nodes. Note, in both (a) and (b), run-time is specified per set of 2 compute nodes, with each compute node containing 24 cores. The total hours per job would be the run-time multiplied by 48.

3.3 Timing Results

The timing results for the composite viscosity models are plotted in Fig. 8(a). Each model was run on 2 compute nodes of the geosolver cluster partition at the Center for Computational Research at the University at Buffalo. Each compute node contains 2 Intel Xeon Gold 6126 processors with 12 cores per processor, making a total of 24 cores per node. Thus, the total hours per job would be the given run-time multiplied by 48. The timing results show that the run-time increases with decreasing plate interface coupling. The model with an initial dip 30° and weakest plate coupling had the highest run-time of 72.72 hours per 2 compute nodes. Whereas, the model with the strongest plate coupling bound and initial dip of 30° took 38.40 hours per 2 compute nodes. The model with an initial dip of 60° and strongest plate coupling bound ran the fastest, finishing in 38.10 hours per 2 compute nodes. The difference in wall-clock time between the models with the weakest and the strongest plate coupling bounds is 89.3%, 47.6%, and 15.9% for models with an initial slab dip of 30°, 45°, and 60°, respectively.

The timing results also show that the greater the peak LAB thickness over time, the higher the runtime (Fig. 8(b)). The model with the longest runtime (over 70 hours per 2 compute nodes) had an initial slab dip of 30° and the weakest plate coupling bound (3.1×10^{20} $Pa \cdot s$). Models with an initial slab dip of 30° and the two strongest plate coupling bounds (and that also have no weakening below 10^{19} $Pa \cdot s$) have a runtime of between 35 and 45 hours. Models with an initial slab dip of 60° and the strongest plate coupling bounds have the shortest runtime (below 40 hours per 2 compute nodes) and the peak thickness below 25 km.

4 Discussion

4.1 Trade-off in Driving Forces and Implications for the Nature of the LAB

The evolution of the slab depends, to a first order, on the balance of the driving and resisting forces acting at subduction zones (Forsyth & Uyeda, 1975; Stern, 2002). Due to the slab's negative buoyancy, slab pull is the primary driving force (Forsyth &

Uyeda, 1975; Billen, 2008). Major resisting forces include mechanical coupling between the plates at the plate interface, the down-going plate's resistance to bending, the viscous resistance of the asthenosphere, and effects at the transition zone (Forsyth & Uyeda, 1975; Billen, 2008; Lallemand et al., 2005; Capitanio et al., 2009; Gerya, 2011).

In this study, we varied the upper bound on the long-term plate interface coupling to investigate how the asthenospheric viscosity below the plates and around the slab changed in response to resisting forces at the plate interface (Fig. 9). The weakening in the LAB region and around the slab dynamically emerged in the models, due to the effects of the non-Newtonian viscosity, resulting in less resistance to subduction. The amount of resistance at the LAB region, slab tip, sub-slab, and mantle wedge varies over time depending on the initial slab dip and plate coupling bound. The weaker the imposed plate interface coupling, the less resistance to subduction and the greater the plate movement, which in return leads to an amplified effect of more weakening in the LAB region.

The depth of the LAB varies from $\sim 70\ km$ beneath oceanic plates to on the order of 250 km beneath cratons (Rychert & Shearer, 2009; Fischer et al., 2010; Lekic & Romanowicz, 2011; Richards et al., 2020). The definition of the depth of LAB varies across studies. A common definition is the depth of maximum negative seismic velocity gradient (Fischer et al., 2010). Surface wave inversion can constrain the LAB depth, but S (Shear wave) receiver-functions are sensitive to the sharpness of the LAB (Eaton et al., 2009). The thickness of the LAB varies from $\leq 20\ km$ for the wet LAB (relatively sharp) to $> 50\ km$ for the dry LAB (graduational or diffuse) (Eaton et al., 2009). Our models are in broad agreement with the thickness of the LAB. Models with the stronger plate interface coupling and deeper initial slab dip either have thin (sharp) dynamically weakened LAB or do not weaken below $10^{19}\ Pa \cdot s$ through time (Fig. 7(e)). Models with combined shallowest initial slab dip and weakest plate interface coupling have 124.6 km thick dynamically weakened LAB zone (Fig. 7(a)), which would be considered thick for the LAB.

The contrast in viscosity can be up to 10 orders of magnitude between the lithosphere and the low viscosity asthenosphere (Doglioni et al., 2011). The reason for the low viscosity in the asthenosphere can not be explained by variation in temperature and grain size, radial anisotropy, or melt alone (Rychert et al., 2020). Studies show that partial melt can reduce the seismic velocity, but does not lower the viscosity in the low viscosity asthenosphere zone (Hua et al., 2023). Our models show that the plate interface coupling and initial slab dip can affect the thickness of the low viscosity LAB area. The high velocity gradients between the asthenosphere and surface plate movement of the down-going plate reduce the viscosity due to the strain-rate dependent weakening of dislocation creep. The amount of plate movement varies with respect to the surface plate velocity which is correlated to the plate interface coupling and initial slab dip. Thus, the models here indicate the weakening in the LAB can be controlled in part by the interplate coupling.

4.2 Implications of Dynamically Evolving Viscous Support of the Slab

Radial viscosity profile of the mantle can be inferred from observations of glacial isostatic adjustment (GIA) (Mitrovica & Forte, 2004), crustal uplift rates (Adhikari et al., 2021), and geoid anomalies (Mao & Zhong, 2021). Mitrovica and Forte (2004) inferred the mean value of the viscosity in the upper mantle is $4 \times 10^{20}\ Pa \cdot s$. If the little ice-age (LIA) mass anomaly, and its uncertainty are considered, then the upper mantle viscosity is found to be in the range of $6 - 11 \times 10^{19}\ Pa \cdot s$ (Adhikari et al., 2021). Mantle convection models with plate motion history infer the asthenosphere viscosity in the range of $1.3 - 4.2 \times 10^{19}\ Pa \cdot s$ (Mao & Zhong, 2021). Other geoid calculations through mantle convection found the asthenosphere viscosity in a similar range ($< 5.4 - 34 \times 10^{19}\ Pa \cdot s$) (Wang et al., 2019). Mantle flow modeling combined with azimuthal

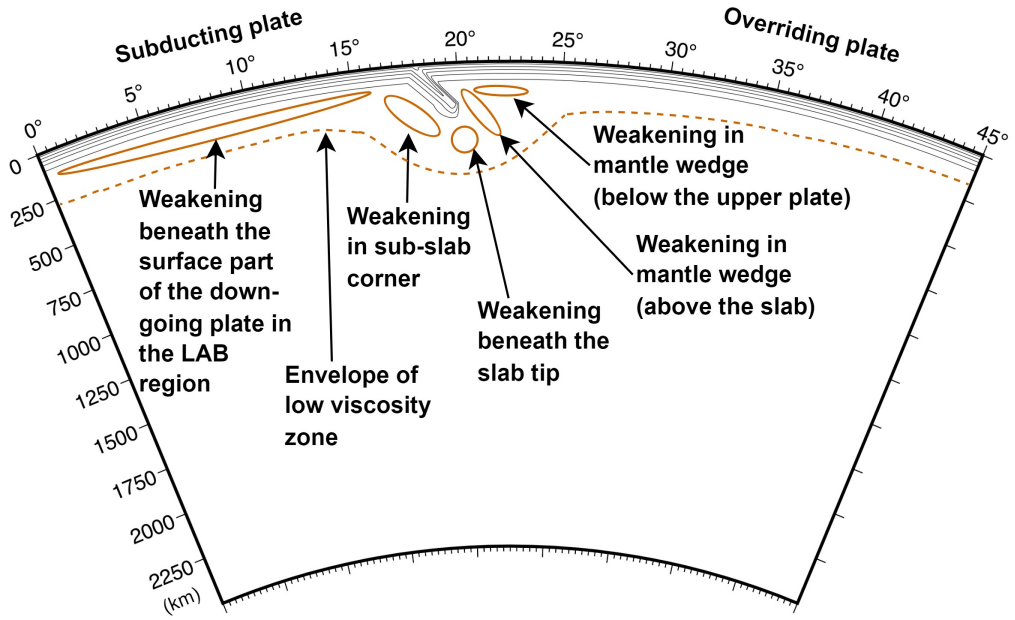

Figure 9: Schematic diagram of the zone of dynamic weakening around the slab and in the LAB region beneath the down-going plate.

seismic anisotropy and plate motions also infer a weak asthenosphere (Becker, 2017). Considering the time-scale (frequency) of the loading/forcing ice masses, the viscosity at 200 km depth (below the seismic LAB) varies from on the order of 10^{18} $Pa{\cdot}s$ (for 10-30 years frequency) to 10^{20} $Pa \cdot s$ (for 10-20 thousand years frequency) (Paxman et al., 2023). The upper mantle viscosity inferred by GIA and geophysical observations fit well when dislocation creep combined with diffusion creep is used (Garel et al., 2020).

The models for the parameter sweep of subduction models presented here suggest that lateral variations in the viscosity of the asthenosphere may be a common phenomenon. This is consistent with previous 2D and 3D models of subduction using a composite viscosity that also predict asthenospheric viscosity values locally as low as 10^{18} $Pa \cdot s$ to 10^{19} $Pa{\cdot}s$ (Jadamec & Billen, 2012; Jadamec, 2016a). The locally emergent viscosity reduction in the numerical models of subduction extends on the order of 500 km laterally from the slab, but this can vary due to initial slab dip and plate interface coupling bound. These values are lower than the global average upper mantle viscosity profiles, suggesting the subduction induced reduction in asthensopheric viscosity is significant for the force balance on subduction, but may be a localized mantle feature.

4.3 Implications for the Surface Motion of Tectonic Plates

Inter-plate coupling is a resisting force that is imposed in this study, whereas, the results show that, with the incorporation of the composite viscosity, the mantle's viscous support is a resisting force that dynamically evolves. Previous results show that the viscous support of the slab affects the surface plate velocity and slab detachment (Andrews & Billen, 2009; Burkett & Billen, 2009). We examine the connection between these resisting forces and surface plate velocity (Fig. 3(d)). The results show that the surface plate velocity and the thickness of the dynamically weakened LAB area are positively correlated; the greater the thickness of the weakened LAB area, the faster the surface plate velocity.

The models show that the average surface plate velocity is faster in the presence of local weakening at the LAB region. The instantaneous models with an initial slab dip of 60° are therefore faster than the models with an initial slab dip of 30°, even though there is less weakening present beneath the slab tip for the models with an initial slab dip of 60°, because the instantaneous models with the initial slab dip of 60° have more weakening in the LAB region. This is true for all instantaneous models with an initial slab dip of 30° and 60°, except for the models with the strongest imposed plate coupling bound ($1 \times 10^{23}\ Pa \cdot s$) (Table 4). For models with an imposed plate coupling bound of $1 \times 10^{23}\ Pa \cdot s$, models with an initial slab dip of 30° and 60° failed to weaken below $1{\times}10^{19}\ Pa{\cdot}s$ in the LAB area. The time-dependent models show that for models with an initial slab dip of 30°, the surface plate velocity continuously increases and has the fastest velocity, unlike the instantaneous models. The slab in models with an initial slab dip of 30° becomes less coupled to the overriding plate over time as it steepens in dip in the time-dependent models, and continues to weaken the LAB region as it subducts.

An increase in surface plate motion with a decrease in plate interface coupling is consistent with the previous analogue studies that show that decreasing mechanic coupling increases subduction velocity (Duarte et al., 2013, 2015; Osei Tutu et al., 2018). However, the results here and in Osei Tutu et al. (2018) also show that the incorporation of strain-rate dependent viscosity results in enhanced weakening in the LAB region that, in turn, can lead to an increase in surface plate velocity as the plate interface coupling is decreased. Thus, models using Newtonian viscosity in the asthenosphere may under-predict surface plate motion. The models here also highlight how the effect of the variation in imposed plate coupling trades off with the initial slab dip. The models here show that for instantaneous models (Jadamec, 2016b; MacDougall et al., 2017), those initiating with a shallower slab dip may have slower initial surface plate motion because there is initially less dynamic weakening in the LAB area. However, the results here show that over time, the models with the shallowest initial slab dip resulted in the fastest surface plate motions due to the dynamic development of weakened LAB area over time.

Modern subducting plate velocity magnitudes varies from 0 to approximately 10 cm/yr on the Earth (Schellart & Rawlinson, 2013). The range of observed velocities are consistent with the results presented here, except for the set of time-dependent models with an initial slab dip of 30° and imposed plate coupling bound of $3.1{\times}10^{20}$ and $1{\times}10^{21}\ Pa{\cdot}s$, which exceed the values observed in plate motions on earth today. Here, for the models with the weakest plate interface and shallowest initial slab dip, the surface plate velocity continuously increases with time which may not occur in modern systems. However, in earlier tectonics (64-56 Ma), the Indian plate speed may have exceeded plate velocities of 18 cm/yr before the collision with Asia plate (Jurdy & Gordon, 1984; Kumar et al., 2007; Capitanio, Morra, et al., 2010; Behr & Becker, 2018). However, the mechanism for faster subduction rate provided here and the mechanism for fast India plate provided by researchers such as loss of lithospheric roots (Kumar et al., 2007), double subduction (Jagoutz et al., 2015), and combination of double subduction and plume push (Pusok & Stegman, 2020) are not necessarily the same.

An implication of the faster subduction velocity, associated with the reduced interplate coupling and thicker weakened LAB, is that the volume of subducted oceanic material will vary over time due in part to the strain-rate dependent viscosity. This is shown in figure 7(b,d,f). As the surface plate velocity increases over time, the depth of the slab tip also increases with time, indicating more subducted material over time when a composite viscosity structure is taken into account.

4.4 Model Limitations

In terms of model limitations, our models do not take into account how the 660 km discontinuity can affect the speed of the descending plate. Previous models indicate that

when the slab tip reaches the discontinuity at 660 km, it can penetrate into the lower mantle or lay on the lower mantle boundary and stagnate at the base of the upper mantle (Goes et al., 2017; Čížková et al., 2007; Lallemand et al., 2005; Fukao & Obayashi, 2013; Sharples et al., 2014; Gerya, 2011). In this study, the initial slab depth is short, but approaches the 660 discontinuity over time. Thus although other locations of the slabs that are short do occur on Earth (e.g. Alaska, Ryukyu, Lesser Antilles, and New-Hebrides subduction zones) (Hayes et al., 2018; Lallemand et al., 2005), when the deep slab and slab behaviors at discontinuity are taken into account, plate speed may be lower than what our models predicted (Billen & Arredondo, 2018). The models in this study also fix the trench location, and thus do not allow for the effects of trench advance or retreat.

2D models with simplified geometry were utilized in this study, and therefor did not account for the variations in the third dimension of plate interface coupling along the trench. However, in 3D models, the varying coupling along the trench can have different effects on the upper plate, as demonstrated in the central versus south Andes in Sobolev and Babeyko (2005) and Alaska (Haynie, 2019). In addition, the growth or reduction of grain size may influence rheology and lead to localized weakening in the mantle (Bercovici & Ricard, 2005, 2014; Mulyukova & Bercovici, 2019). While incorporating non-Newtonian viscosity into the model presents its own challenges, the models here did not include grain size variation.

Lastly, the presence of significant viscosity gradients within an element poses challenges for solvers and can impact solution time (Moresi et al., 1996; Moresi & Solomatov, 1995; Jadamec et al., 2012). Smaller viscosity contrasts (May & Moresi, 2008) and smaller stress variations in the upper mantle (Rudi et al., 2022), lead to faster convergence rates. In our study, models with a weaker plate interface exhibited longer runtimes. The presence of large viscosity gradients arises due to dynamically emergent weakening in the LAB region and around the subducting slab. As the plate interface coupling decreases, the dynamic weakening intensifies, resulting in an increase in runtime.

5 Conclusion

On Earth, subduction zones have a variation of slab dips and magnitudes of plate interface coupling. However, defining the subduction interface is challenging, and how plate coupling affects the long-term subduction dynamics is still not well understood. A systematic study of 2D time-dependent models varying six values of plate interface coupling and three values of initial slab dip were run for 2000 time-steps. The surface plate velocity and the thickness of the dynamically weakened LAB were examined. The models show that surface plate velocity increases with decreasing plate interface coupling. For the instantaneous models, the surface plate velocity peaks for the slab with an initial dip of 45°. In the time-dependent models, the models with an initial slab dip of 30° have the fastest surface plate motion. The results show that thickness of the dynamically weakened LAB and plate interface coupling are interrelated such that the weaker the inter-plate coupling, the thicker the dynamic weakening. The maximum thickness of the weakened LAB area achieved is over 120 km by the model with an initial slab dip of 30° and plate coupling bound of 3.1×10^{20} $Pa{\cdot}s$. The surface plate velocity and dynamic weakening in LAB are also positively correlated. Greater dynamic weakening allows for a faster subduction plate speed, indicating models that use only a Newtonian viscosity may under-predict surface plate motions. The reduced viscous resistance to slab sinking facilitates subducting plate motion and mantle flow velocities over time, thus may be a critical factor in allowing subduction to occur on Earth. Thus, the models show that the dynamically weakened LAB region may be important for facilitating the motion of the surface plates.

Data Availability Statement The CitcomCU source code used to run the models is available at `https://github.com/vbhavsar16/CitcomCU_vbh23`

Acknowledgments

This work is supported by NSF CAREER Award 1945513 awarded to M. Jadamec and by U.S. DOE Contract DE-AC02-06CH11357 awarded to M. Knepley. M. Knepley and V. Bhavsar were also partially supported by NSF EAR-0949446 (The Computational Infrastructure for Geodynamics project). V. Bhavsar also received a Pegrum Professional Development Award from the Department of Geology at the University at Buffalo. The numerical simulations were run on Jadamec-Knepley 1200-core geosolver partition at the University at Buffalo's Center for Computational Research (Center for Computational Research, University at Buffalo, 2020). We thank the staff at the University at Buffalo's Center for Computational Research for cluster support.

References

Adhikari, S., Milne, G., Caron, L., Khan, S., Kjeldsen, K., Nilsson, J., ... Ivins, E. (2021). Decadal to centennial timescale mantle viscosity inferred from modern crustal uplift rates in Greenland. *Geophysical Research Letters*, *48*(19), e2021GL094040.

Agard, P., Plunder, A., Angiboust, S., Bonnet, G., & Ruh, J. (2018). The subduction plate interface: Rock record and mechanical coupling (from long to short timescales). *Lithos*, *320*, 537–566.

Andrews, E. R., & Billen, M. I. (2009). Rheologic controls on the dynamics of slab detachment. *Tectonophysics*, *464*(1-4), 60–69.

Becker, T. W. (2017). Superweak asthenosphere in light of upper mantle seismic anisotropy. *Geochemistry, Geophysics, Geosystems*, *18*(5), 1986–2003.

Behr, W. M., & Becker, T. W. (2018). Sediment control on subduction plate speeds. *Earth and Planetary Science Letters*, *502*, 166–173.

Bercovici, D. (2003). The generation of plate tectonics from mantle convection. *Earth and Planetary Science Letters*, *205*(3-4), 107–121.

Bercovici, D., & Ricard, Y. (2005). Tectonic plate generation and two-phase damage: Void growth versus grain size reduction. *Journal of Geophysical Research: Solid Earth*, *110*(B3).

Bercovici, D., & Ricard, Y. (2014). Plate tectonics, damage and inheritance. *Nature*, *508*(7497), 513–516.

Billen, M. I. (2008). Modeling the dynamics of subducting slabs. *Annu. Rev. Earth Planet. Sci.*, *36*, 325–356.

Billen, M. I., & Arredondo, K. M. (2018). Decoupling of plate-asthenosphere motion caused by non-linear viscosity during slab folding in the transition zone. *Physics of the Earth and Planetary Interiors*, *281*, 17–30.

Billen, M. I., & Gurnis, M. (2001). A low viscosity wedge in subduction zones. *Earth and Planetary Science Letters*, *193*(1-2), 227–236.

Billen, M. I., & Hirth, G. (2007). Rheologic controls on slab dynamics. *Geochemistry, Geophysics, Geosystems*, *8*(8).

Burkett, E. R., & Billen, M. I. (2009). Dynamics and implications of slab detachment due to ridge-trench collision. *Journal of Geophysical Research: Solid Earth*, *114*(B12).

Capitanio, F. A., & Faccenda, M. (2012). Complex mantle flow around heterogeneous subducting oceanic plates. *Earth and Planetary Science Letters*, *353*, 29–37.

Capitanio, F. A., Morra, G., & Goes, S. (2009). Dynamics of plate bending at the trench and slab-plate coupling. *Geochemistry, Geophysics, Geosystems*, *10*(4).

Capitanio, F. A., Morra, G., Goes, S., Weinberg, R., & Moresi, L.-N. (2010). India-Asia convergence driven by the subduction of the Greater Indian continent. *Nature Geoscience*, *3*(2), 136–139.

Capitanio, F. A., Stegman, D. R., Moresi, L.-N., & Sharples, W. (2010). Upper plate controls on deep subduction, trench migrations and deformations at convergent

margins. *Tectonophysics*, *483*(1-2), 80–92.

Center for Computational Research, University at Buffalo. (2020). *UB CCR Support Portfolio.* (`http://hdl.handle.net/10477/79221`)

Čížková, H., van Hunen, J., & van den Berg, A. (2007). Stress distribution within subducting slabs and their deformation in the transition zone. *Physics of the Earth and Planetary Interiors*, *161*(3-4), 202–214.

Doglioni, C., Ismail-Zadeh, A., Panza, G., & Riguzzi, F. (2011). Lithosphere-asthenosphere viscosity contrast and decoupling. *Physics of the Earth and Planetary Interiors*, *189*(1-2), 1–8.

Duarte, J. C., Schellart, W. P., & Cruden, A. R. (2013). Three-dimensional dynamic laboratory models of subduction with an overriding plate and variable interplate rheology. *Geophysical Journal International*, *195*(1), 47–66.

Duarte, J. C., Schellart, W. P., & Cruden, A. R. (2015). How weak is the subduction zone interface? *Geophysical Research Letters*, *42*(8), 2664–2673.

Eaton, D. W., Darbyshire, F., Evans, R. L., Grütter, H., Jones, A. G., & Yuan, X. (2009). The elusive lithosphere–asthenosphere boundary (LAB) beneath cratons. *Lithos*, *109*(1-2), 1–22.

Fischer, K. M., Ford, H. A., Abt, D. L., & Rychert, C. A. (2010). The lithosphere-asthenosphere boundary. *Annual Review of Earth and Planetary Sciences*, *38*, 551–575.

Forsyth, D., & Uyeda, S. (1975). On the relative importance of the driving forces of plate motion. *Geophysical Journal International*, *43*(1), 163–200.

Fukao, Y., & Obayashi, M. (2013). Subducted slabs stagnant above, penetrating through, and trapped below the 660 km discontinuity. *Journal of Geophysical Research: Solid Earth*, *118*(11), 5920–5938.

Gao, S. (2018). Dynamic asthenospheric weakening facilitating plate tectonic motion. *Master's Thesis*.

Garel, F., Thoraval, C., Tommasi, A., Demouchy, S., & Davies, D. R. (2020). Using thermo-mechanical models of subduction to constrain effective mantle viscosity. *Earth and Planetary Science Letters*, *539*, 116243.

Gerya, T. (2011). Future directions in subduction modeling. *Journal of Geodynamics*, *52*(5), 344–378.

Gerya, T., Connolly, J. A., & Yuen, D. A. (2008). Why is terrestrial subduction one-sided? *Geology*, *36*(1), 43–46.

Goes, S., Agrusta, R., van Hunen, J., & Garel, F. (2017). Subduction-transition zone interaction: A review. *Geosphere*, *13*(3), 644–664.

Gutscher, M. A., Spakman, W., Bijwaard, H., & Engdahl, E. R. (2000). Geodynamics of flat subduction: Seismicity and tomographic constraints from the Andean margin. *Tectonics*, *19*(5), 814-833.

Hall, C. E., & Parmentier, E. (2003). Influence of grain size evolution on convective instability. *Geochemistry, Geophysics, Geosystems*, *4*(3).

Hayes, G. P., Moore, G. L., Portner, D. E., Hearne, M., Flamme, H., Furtney, M., & Smoczyk, G. M. (2018). Slab2, a comprehensive subduction zone geometry model. *Science*, *362*(6410), 58–61.

Haynie, K. L. (2019). Controls of flat slab versus oceanic plateau subduction on overriding plate deformation in south-central Alaska. *Ph. D. Thesis*.

Hirth, G., & Kohlstedt, D. (2003). Rheology of the upper mantle and the mantle wedge: A view from the experimentalists. *Geophysical monograph-american geophysical union*, *138*, 83–106.

Hirth, G., & Kohlstedt, D. (2004). Rheology of the upper mantle and the mantle wedge: A view from the experimentalists. *Inside the subduction Factory*, *138*, 83–105.

Hua, J., Fischer, K. M., Becker, T. W., Gazel, E., & Hirth, G. (2023). Asthenospheric low-velocity zone consistent with globally prevalent partial melting. *Nature Geoscience*, *16*(2), 175–181.

Huang, S., Sacks, I. S., & Snoke, J. A. (1998). Compressional deformation of island-arc lithosphere in northeastern Japan resulting from long-term subduction-related tectonic forces: Finite-element modeling. *Tectonophysics*, *287*(1-4), 43–58.

Jadamec, M. A. (2009). Three-dimensional lithosphere and mantle dynamics: Models of the subduction-transform plate boundary system in southern Alaska. *ProQuest Dissertations and Theses*, 165. Retrieved from `https://www.proquest.com/dissertations-theses/three-dimensional-lithosphere-mantle-dynamics/docview/304854195/se-2?accountid=14169`

Jadamec, M. A. (2015). Slab-driven mantle weakening and rapid mantle flow. *Subduction Dynamics: From Mantle Flow to Mega Disasters*, *211*, 135.

Jadamec, M. A. (2016a). Insights on slab-driven mantle flow from advances in three-dimensional modelling. *Journal of Geodynamics*, *100*, 51–70.

Jadamec, M. A. (2016b). Slab-driven mantle weakening and rapid mantle flow. *Subduction Dynamics: From Mantle Flow to Mega Disasters, Geophys. Monogr. Ser*, 135–155.

Jadamec, M. A., & Billen, M. I. (2010). Reconciling surface plate motions with rapid three-dimensional mantle flow around a slab edge. *Nature*, *465*(7296), 338.

Jadamec, M. A., & Billen, M. I. (2012). The role of rheology and slab shape on rapid mantle flow: Three-dimensional numerical models of the Alaska slab edge. *Journal of Geophysical Research: Solid Earth*, *117*(B2).

Jadamec, M. A., Billen, M. I., & Kreylos, O. (2012). Three-dimensional simulations of geometrically complex subduction with large viscosity variations. In *Proceedings of the 1st conference of the extreme science and engineering discovery environment: Bridging from the extreme to the campus and beyond* (p. 31).

Jadamec, M. A., Kreylos, O., Chang, B., Fischer, K. M., & Yikilmaz, M. B. (2018). A visual survey of global slab geometries with ShowEarthModel and implications for a three-dimensional subduction paradigm. *Earth and Space Science*, *5*(6), 240–257.

Jagoutz, O., Royden, L., Holt, A. F., & Becker, T. W. (2015). Anomalously fast convergence of India and Eurasia caused by double subduction. *Nature Geoscience*, *8*(6), 475–478.

Jarrard, R. D. (1986). Relations among subduction parameters. *Reviews of Geophysics*, *24*(2), 217-284.

Jurdy, D. M., & Gordon, R. G. (1984). Global plate motions relative to the hot spots 64 to 56 Ma. *Journal of Geophysical Research: Solid Earth*, *89*(B12), 9927–9936.

Kneller, E. A., & Van Keken, P. E. (2007). Trench-parallel flow and seismic anisotropy in the Mariana and Andean subduction systems. *Nature*, *450*(7173), 1222–1225.

Kumar, P., Yuan, X., Kumar, M. R., Kind, R., Li, X., & Chadha, R. (2007). The rapid drift of the Indian tectonic plate. *Nature*, *449*(7164), 894–897.

Lallemand, S., Heuret, A., & Boutelier, D. (2005). On the relationships between slab dip, back-arc stress, upper plate absolute motion, and crustal nature in subduction zones. *Geochemistry, Geophysics, Geosystems*, *6*(9).

Lamb, S., & Davis, P. (2003). Cenozoic climate change as a possible cause for the rise of the Andes. *Nature*, *425*(6960), 792–797.

Lekic, V., & Romanowicz, B. (2011). Tectonic regionalization without a priori information: A cluster analysis of upper mantle tomography. *Earth and Planetary Science Letters*, *308*(1-2), 151–160.

Li, C., van der Hilst, R. D., Engdahl, E. R., & Burdick, S. (2008). A new global model for P wave speed variations in Earth's mantle. *Geochemistry, Geophysics, Geosystems*, *9*(5).

Long, M. D., & Silver, P. G. (2008). The subduction zone flow field from seismic

anisotropy: A global view. *science*, *319*(5861), 315–318.

MacDougall, J. G., Jadamec, M. A., & Fischer, K. M. (2017). The zone of influence of the subducting slab in the asthenospheric mantle. *Journal of Geophysical Research: Solid Earth*, *122*(8), 6599–6624.

Mao, W., & Zhong, S. (2021). Constraints on mantle viscosity from intermediate-wavelength geoid anomalies in mantle convection models with plate motion history. *Journal of Geophysical Research: Solid Earth*, *126*(4), e2020JB021561.

May, D. A., & Moresi, L.-N. (2008). Preconditioned iterative methods for Stokes flow problems arising in computational geodynamics. *Physics of the Earth and Planetary Interiors*, *171*(1-4), 33–47.

McKenzie, D. P., Roberts, J. M., & Weiss, N. O. (1974). Convection in the Earth's mantle: Towards a numerical simulation. *Journal of fluid mechanics*, *62*(3), 465–538.

Mitrovica, J., & Forte, A. (2004). A new inference of mantle viscosity based upon joint inversion of convection and glacial isostatic adjustment data. *Earth and Planetary Science Letters*, *225*(1-2), 177–189.

Moresi, L.-N., & Solomatov, V. (1995). Numerical investigation of 2D convection with extremely large viscosity variations. *Physics of Fluids*, *7*(9), 2154–2162.

Moresi, L.-N., Zhong, S., & Gurnis, M. (1996). The accuracy of finite element solutions of Stokes's flow with strongly varying viscosity. *Physics of the Earth and Planetary Interiors*, *97*(1-4), 83–94.

Mulyukova, E., & Bercovici, D. (2019). The generation of plate tectonics from grains to global scales: A brief review. *Tectonics*, *38*(12), 4058–4076.

Osei Tutu, A., Sobolev, S. V., Steinberger, B., Popov, A. A., & Rogozhina, I. (2018). Evaluating the influence of plate boundary friction and mantle viscosity on plate velocities. *Geochemistry, Geophysics, Geosystems*, *19*(3), 642–666.

Paxman, G. J., Lau, H. C., Austermann, J., Holtzman, B. K., & Havlin, C. (2023). Inference of the timescale-dependent apparent viscosity structure in the upper mantle beneath Greenland. *AGU Advances*, *4*(2), e2022AV000751.

Pusok, A. E., & Stegman, D. R. (2020). The convergence history of India-Eurasia records multiple subduction dynamics processes. *Science Advances*, *6*(19), eaaz8681.

Richards, F., Hoggard, M., Crosby, A., Ghelichkhan, S., & White, N. (2020). Structure and dynamics of the oceanic lithosphere-asthenosphere system. *Physics of the Earth and Planetary Interiors*, *309*, 106559.

Romanowicz, B. (2009). The thickness of tectonic plates. *Science*, *324*(5926), 474–476.

Rudi, J., Gurnis, M., & Stadler, G. (2022). Simultaneous inference of plate boundary stresses and mantle rheology using adjoints: Large-scale 2-D models. *Geophysical Journal International*, *231*(1), 597–614.

Rychert, C. A., Harmon, N., Constable, S., & Wang, S. (2020). The nature of the lithosphere-asthenosphere boundary. *Journal of Geophysical Research: Solid Earth*, *125*(10), e2018JB016463.

Rychert, C. A., & Shearer, P. M. (2009). A global view of the lithosphere-asthenosphere boundary. *Science*, *324*(5926), 495–498.

Schellart, W. P., & Rawlinson, N. (2013). Global correlations between maximum magnitudes of subduction zone interface thrust earthquakes and physical parameters of subduction zones. *Physics of the Earth and Planetary Interiors*, *225*, 41–67.

Semple, A., & Lenardic, A. (2021). Feedbacks between a non-Newtonian upper mantle, mantle viscosity structure and mantle dynamics. *Geophysical Journal International*, *224*(2), 961–972.

Sharples, W., Jadamec, M. A., Moresi, L.-N., & Capitanio, F. A. (2014). Overriding plate controls on subduction evolution. *Journal of Geophysical Research: Solid*

Earth, *119*(8), 6684–6704.
Sharples, W., Moresi, L.-N., Velic, M., Jadamec, M. A., & May, D. A. (2016). Simulating faults and plate boundaries with a transversely isotropic plasticity model. *Physics of the Earth and Planetary Interiors*, *252*, 77–90.
Shreve, R. L., & Cloos, M. (1986). Dynamics of sediment subduction, melange formation, and prism accretion. *Journal of Geophysical Research: Solid Earth*, *91*(B10), 10229–10245.
Sobolev, S. V., & Babeyko, A. Y. (2005). What drives orogeny in the Andes? *Geology*, *33*(8), 617–620.
Stadler, G., Gurnis, M., Burstedde, C., Wilcox, L. C., Alisic, L., & Ghattas, O. (2010). The dynamics of plate tectonics and mantle flow: From local to global scales. *Science*, *329*(5995), 1033–1038.
Stern, R. J. (2002). Subduction zones. *Reviews of geophysics*, *40*(4), 3–1.
Syracuse, E. M., & Abers, G. A. (2006). Global compilation of variations in slab depth beneath arc volcanoes and implications. *Geochemistry, Geophysics, Geosystems*, *7*(5).
Tagawa, M., Nakakuki, T., Kameyama, M., & Tajima, F. (2007). The role of history-dependent rheology in plate boundary lubrication for generating one-sided subduction. *Pure and Applied Geophysics*, *164*(5), 879–907.
Torrance, K., & Turcotte, D. (1971). Thermal convection with large viscosity variations. *Journal of Fluid Mechanics*, *47*(1), 113–125.
Tovish, A., Schubert, G., & Luyendyk, B. P. (1978). Mantle flow pressure and the angle of subduction: Non-Newtonian corner flows. *Journal of Geophysical Research: Solid Earth*, *83*(B12), 5892–5898.
Uyeda, S., & Kanamori, H. (1979). Back-arc opening and the mode of subduction. *Journal of Geophysical Research: Solid Earth*, *84*(B3), 1049–1061.
van Keken, P. E., Currie, C., King, S. D., Behn, M. D., Cagnioncle, A., He, J., ... others (2008). A community benchmark for subduction zone modeling. *Physics of the Earth and Planetary Interiors*, *171*(1-4), 187–197.
Wada, I., & Wang, K. (2009). Common depth of slab-mantle decoupling: Reconciling diversity and uniformity of subduction zones. *Geochemistry Geophysics Geosystems*, *10*(10), Q10009.
Wang, X., Holt, W. E., & Ghosh, A. (2019). Joint modeling of lithosphere and mantle dynamics: Sensitivity to viscosities within the lithosphere, asthenosphere, transition zone, and D" layers. *Physics of the Earth and Planetary Interiors*, *293*, 106263.
Wdowinski, S., O'Connell, R. J., & England, P. (1989). A continuum model of continental deformation above subduction zones: Application to the Andes and the Aegean. *Journal of Geophysical Research: Solid Earth*, *94*(B8), 10331–10346.
Yang, T., & Gurnis, M. (2016). Dynamic topography, gravity and the role of lateral viscosity variations from inversion of global mantle flow. *Geophysical Supplements to the Monthly Notices of the Royal Astronomical Society*, *207*(2), 1186–1202.
Zhong, S. (2006). Constraints on thermochemical convection of the mantle from plume heat flux, plume excess temperature, and upper mantle temperature. *Journal of Geophysical Research: Solid Earth*, *111*(B4).
Zhong, S., Yuen, D., Moresi, L.-N., & Knepley, M. (2015). Numerical methods for mantle convection. *Treatise on Geophysics (Second Edition), edited by: Schubert, G., Elsevier, Oxford*, *2*, 197–222.